

Faithful, Interpretable Chest X-ray Diagnosis with Anti-Aliased B-cos Networks

Marcel Kleinmann¹ Shashank Agnihotri¹ Margret Keuper^{1,2}

¹Data and Web Science Group, University of Mannheim, Germany

²Max-Planck-Institute for Informatics, Saarland Informatics Campus, Germany

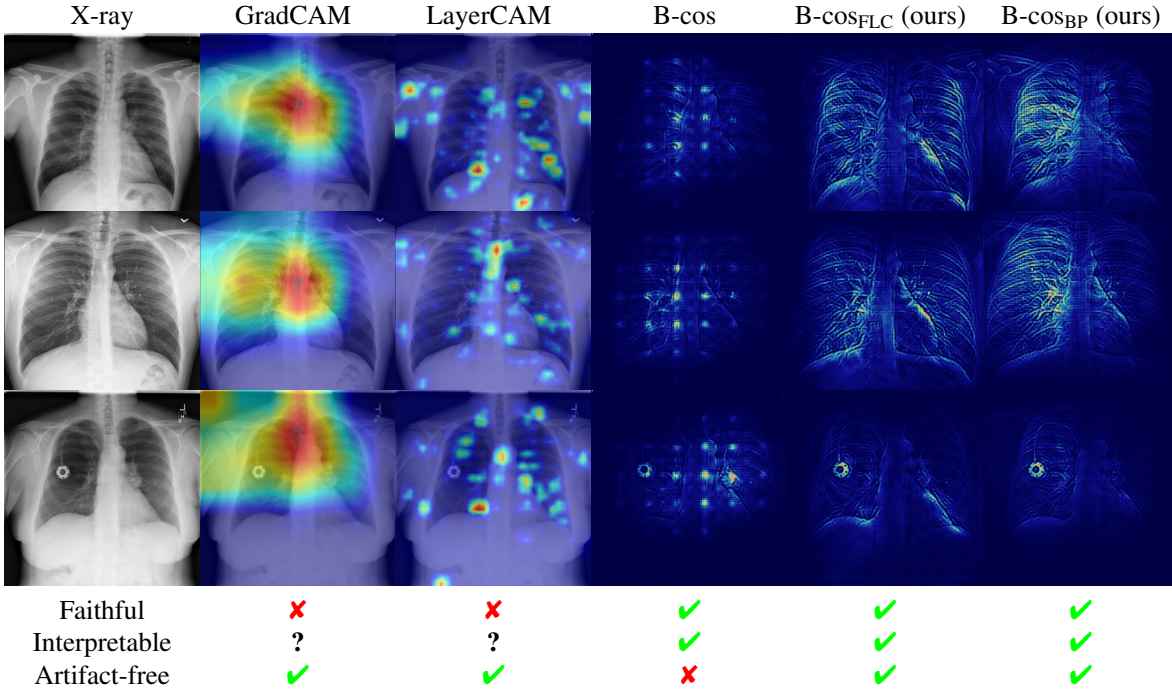


Figure 1. An illustration comparing our proposed B-cos_{FLC} and B-cos_{BP} approaches with the standard B-cos explanation and other widely used post-hoc explanation methods, such as GradCAM [50] and LayerCAM [29], highlighting their respective advantages.

Abstract

Faithfulness and interpretability are essential for deploying deep neural networks (DNNs) in safety-critical domains such as medical imaging. B-cos networks offer a promising solution by replacing standard linear layers with a weight-input alignment mechanism, producing inherently interpretable, class-specific explanations without post-hoc methods. While maintaining diagnostic performance competitive with state-of-the-art DNNs, standard B-cos models suffer from severe aliasing artifacts in their explanation maps, making them unsuitable for clinical use where clarity is essential. Additionally, the original B-cos formulation is limited to multi-class settings, whereas chest X-ray analysis often requires multi-label classification due to co-occurring abnormalities. In this work, we address both limitations: (1) we introduce anti-aliasing strategies using FLCPooling (FLC) and BlurPool (BP) to significantly im-

prove explanation quality, and (2) we extend B-cos networks to support multi-label classification. Our experiments on chest X-ray datasets demonstrate that the modified B-cos_{FLC} and B-cos_{BP} preserve strong predictive performance while providing faithful and artifact-free explanations suitable for clinical application in multi-label settings. Code available at: [GitHub repository](#).

1. Introduction

Faithfulness and interpretability are critical prerequisites for deploying deep learning models in safety-critical domains such as healthcare, where decisions have direct implications for patient outcomes [49, 61]. In particular, clinical adoption demands models whose reasoning processes can be understood and verified by medical professionals. However, most existing approaches in medical image processing rely on architectures that lack inherent interpretability, of-

ferring limited insight into the basis of their predictions [42]. As emphasized in [61], knowing how a diagnosis was derived is highly valuable, especially in practice, where AI tools are used to support, not replace, radiologists. In this work, we explore B-cos networks [8], which are inherently interpretable by design and generate class-specific contribution maps that visually indicate the evidence behind each prediction. Representative examples are shown in Fig. 1 which compares our artifact-free, faithful and interpretable explanations to other common approaches such as Grad-CAM and LayerCAM while displaying the need for our extensions when working with B-cos networks and chest X-rays simultaneously.

These models can directly show which part of the image caused network activations, enabling an understanding of why a classification was made [8]. Unlike post-hoc approaches such as GradCAM [50] or LayerCAM [29], which provide coarse and sometimes misleading heatmaps that have insufficient mechanistic explanation of the decision-making process [17, 48], B-cos networks offer inherently interpretable, class-specific contribution maps that yield clearer, more faithful visual explanations. This can help radiologists verify predictions, improve clinical workflows, and reduce diagnostic errors. However, standard B-cos models face two critical limitations: first, the generated explanation maps often exhibit grid artifacts, making them visually unreliable for clinical use; second, the original formulation supports only multi-class classification, whereas chest X-rays commonly involve multiple co-occurring conditions. In this work, we address both limitations by incorporating anti-aliasing techniques such as FLCPooling and BlurPool to improve visual clarity, and by extending the B-cos framework to support multi-label classification. We refer to the resulting anti-aliased, multi-label capable model as B-cos_{FLC} and B-cos_{BP}. While B-cos_{FLC} combines B-cos models with FLCPooling [22], B-cos_{BP} combines it with BlurPooling [59], both effective anti-aliasing techniques. These anti-aliasing techniques help improve the explanation maps from the B-cos network, since they replace the artifact-producing downsampling operation with an artifact-free downsampling path. Thus, removing the artifacts in the explanation maps of B-Cos networks. Our main contributions are:

- A practical evaluation of B-cos networks for interpretable and clinically relevant chest X-ray disease detection.
- Application-specific modifications to B-cos networks by integrating anti-aliasing methods (FLCPooling and BlurPool) to produce spectral artifact-free explanations suitable for diagnostic use.
- An extension of the B-cos framework to multi-label classification, addressing the clinical need to detect

multiple co-existing conditions in a single chest radiograph.

2. Related Work

To contextualize the proposed approach, we review prior work across three key areas: clinical evaluation criteria in medical imaging, deep learning methods for chest X-ray disease detection, and approaches to explainability in medical AI systems.

Clinical Evaluation Metrics in Medical Imaging:

While many works in medical imaging rely on standard machine learning metrics [32–34], clinical studies typically assess diagnostic tools using sensitivity and specificity [1, 36, 39]. Sensitivity reflects the proportion of true positive cases correctly identified and corresponds to recall in the machine learning literature. Specificity, in contrast, quantifies the proportion of true negatives correctly classified. In clinical practice, high sensitivity is essential for early disease detection, as delayed diagnosis, particularly in conditions such as pneumonia, can severely impact patient outcomes [31], with reported mortality rates of up to 42% in children [40]. Although specificity is often considered less critical, it is not uncommon to observe high sensitivity levels between 64% and 94%, accompanied by relatively low specificity values between 16% and 67% [40]. This trade-off frequently results in precautionary treatments, which may cause unnecessary anxiety in patients and contribute to antimicrobial resistance. In this work, we place additional emphasis on specificity, as reducing false positives is crucial to building clinical trust and avoiding harmful diagnostic outcomes.

Deep Learning in Medical Imaging: The development of automated abnormality detection systems for chest X-rays dates back several decades, with early rule-based and statistical methods emerging in the 1960s [61]. These early systems were constrained by the limited computational and imaging technology of the time. With the advent of deep learning, chest X-ray analysis has undergone a significant transformation, as modern convolutional and transformer-based models demonstrate performance that often matches or exceeds that of expert radiologists [37]. This progress has been enabled by the availability of large-scale annotated datasets and advances in neural network architectures, positioning deep learning as the dominant approach for chest radiograph interpretation.

Model Architectures: Convolutional neural networks (CNNs) remain the most widely used architectures for chest X-ray classification tasks. ResNet [24], and specifically ResNet50 [24], has been effectively applied to COVID-19 detection on large-scale datasets such as CheXpert [28] and NIH ChestX-ray14 [57], showing high performance [25]. CheXNet [45], based on DenseNet-121 [27], reports a pneumonia detection F1-score of 0.435, surpassing the average

radiologist performance of 0.387 on the same dataset [57]. Lightweight CNN variants such as MobileNet [26] and EfficientNet [46] have also demonstrated competitive results across several datasets [46, 47]. More recently, vision transformers (ViTs) [53]. IEViT [43], a ViT variant designed specifically for medical imaging, further improves upon standard ViTs and achieves F1-scores of up to 100% across four chest X-ray datasets [43].

Datasets: Several benchmark datasets are widely used for chest X-ray analysis, particularly for image classification tasks. NIH ChestX-ray14 [57] is one of the most established datasets, containing 112,120 frontal-view radiographs annotated with 15 unique labels, 14 of which correspond to disease findings. It also includes 880 images with bounding box annotations indicating the disease location. CheXpert [28] is another large-scale dataset with 224,316 radiographs from 65,420 patients. The authors of CheXpert report improved label quality through a rule-based labeler, though both NIH ChestX-ray14 and CheXpert remain widely used in practice [28]. Other datasets such as MIMIC-CXR [30] and PadChest [7] offer similar scale and disease coverage, but are not suitable for our setting due to the absence of bounding box annotations necessary for evaluating localization performance.

For this work, we focus on datasets that provide region-level annotations, which are essential for quantitative assessment of visual explanations. In the single-label setting, we use the RSNA Pneumonia Detection Challenge (2018) dataset [51], which contains 26,684 radiographs annotated as either pneumonia or no pneumonia, along with bounding boxes localizing the affected regions. Despite being designed for a Kaggle challenge, the dataset remains widely used for both image classification and object detection tasks due to its high-quality annotations. For the multi-label setting, we use the VinBigData Chest X-ray Abnormalities Detection dataset, a modified version of VinDr-CXR [41], consisting of 15,000 radiographs with bounding boxes for 14 thoracic abnormalities. This dataset is particularly valuable because all annotations were manually curated by 17 board-certified radiologists [41], ensuring high-quality supervision. Moreover, it reflects realistic clinical cases where multiple pathologies often co-occur within a single image, making it well-suited for the multi-label classification task studied in this work.

Explainable AI in Medical Imaging: Explainability in machine learning refers to the ability to understand and interpret how complex models arrive at their decisions [18]. In safety-critical domains such as medical imaging, the need for transparency is particularly pronounced, as clinical decisions require justification that can be trusted and verified by healthcare professionals [10]. Improving trust, reliability, and acceptance among clinical stakeholders has been shown to directly impact the integration of AI systems in

healthcare settings [10]. Beyond clinical utility, regulatory frameworks such as the European General Data Protection Regulation (GDPR) now require decision traceability, limiting the use of models that do not offer clear reasoning [52].

Two main categories of explainable AI have emerged: post-hoc explanation methods and inherently interpretable models [6]. Post-hoc techniques aim to explain models that were not designed to be interpretable, but these often lack fidelity to the original model and fail to provide reliable insight into the underlying decision process [17, 55]. As a result, their adoption in high-stakes applications remains limited. In contrast, inherently interpretable models, also referred to as transparent or intrinsic models, are designed from the outset to produce faithful and understandable explanations [6, 8]. This perspective is strongly supported in [48], which argues that for high-stakes domains such as healthcare, post-hoc explanations are insufficient and interpretable models should be used instead.

In this work, we follow this paradigm and evaluate B-cos networks [8] as an inherently interpretable architecture for medical imaging tasks, focusing on their suitability for providing clinically meaningful explanations in chest X-ray analysis.

3. Methodology

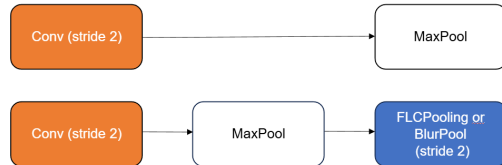


Figure 2. Illustration of the anti-aliasing downsampling strategy adapted from [22, 59]. Instead of applying a convolution with a stride greater than 1 (top path), the operation is decomposed into a stride=1 convolution followed by an anti-aliasing pooling layer (BlurPool or FLCPooling) with the desired stride (bottom path). This modification reduces spectral artifacts by separating the convolution and downsampling operations. The example shown demonstrates the replacement of a stride=2 convolution with a stride=1 convolution followed by a BlurPool or FLCPooling layer with a stride of 2.

In this work, we adopt transfer learning [60] for both baseline and B-cos variants of widely used model architectures in chest X-ray analysis, including ResNet [24] and Vision Transformers (ViT) [14]. Due to the limited size of datasets containing bounding box annotations necessary for explanation analysis, we fine-tune models pre-trained on large-scale datasets. In line with prior work in medical imaging [36], we initialize all models with ImageNet-pretrained weights to ensure strong baseline performance. Additionally, task-specific preprocessing is essential. We adapt a light augmentation strategy from [15],

which demonstrated strong results on the RSNA Pneumonia Detection dataset [51]. Further details are provided in Appendix C.2.

3.1. Extending B-cos for Multi-label Classification

B-cos networks [8] provide inherently interpretable outputs by computing class-specific contribution maps, but are originally designed for multi-class classification. In such cases, only the explanation map corresponding to the predicted class is generated. However, in medical imaging, multiple pathologies often co-occur, making multi-label classification essential. To address this, we extend B-cos to compute contribution maps for all output neurons simultaneously. This enables a full analysis of model behavior across all conditions and does not alter the underlying training or inference pipeline. Instead, it enhances the interpretability by allowing inspection of every class output, which is critical in the medical domain where several diseases can co-occur.

3.2. Removing Artifacts with Anti-Aliased Down-sampling

Although B-cos networks yield human-interpretable contribution maps, we observe that their visual quality is often impaired by aliasing artifacts. These arise due to distortions in the intermediate feature representations caused by strided convolutions, which downsample the feature maps using inefficient sampling strategies that violate the Nyquist theorem [2, 3, 22]. As a result, high-frequency components are undersampled, introducing artifacts that propagate into the explanation maps and limit their clinical usability.

To mitigate this, we adopt anti-aliasing downsampling strategies using either BlurPool [59] or FLCPooling [22, 23]. BlurPool applies a spatial blurring filter before down-sampling, reducing high-frequency noise in the spatial domain. In contrast, FLCPooling applies a principled low-pass filter in the frequency domain to enforce sampling that adheres to the Nyquist criterion. Both methods result in smoother, artifact-free feature representations, thereby improving the visual fidelity and faithfulness of B-cos explanation maps.

The integration of these techniques follows the approach illustrated in Fig. 2. Instead of directly using a convolution with a stride greater than one, we first apply a convolution with a stride of 1, followed by a MaxOut activation and then downsample using either BlurPool or FLCPooling with the original stride. This separation of convolution and downsampling operations ensures that aliasing is minimized during spatial resolution reduction. We refer to our anti-aliased model variant as B-Cos_{FLC}, where FLCPooling and B-Cos_{BP} where BlurPool is also evaluated.

4. Experiments

4.1. Setup

All experiments are conducted using fixed random seeds to ensure full reproducibility. We evaluate on two datasets that provide bounding box annotations: the RSNA Pneumonia Detection Challenge (2018) [51], focused on binary classification (pneumonia vs. no pneumonia), and the Vin-BigData Chest X-ray Abnormalities Detection dataset [41], which enables multi-label classification of 14 thoracic conditions. These bounding box annotations allow for a quantitative assessment of explanation quality in addition to classification performance.

We use five-fold cross-validation [35] to make effective use of limited training data while maintaining sufficient diversity in the test splits. A 20% test split ensures adequate coverage of clinical variability, particularly the range of pneumonia presentations across different lung regions [5]. This protocol also allows for a fair comparison with prior work, including the most cited paper on pneumonia classification, which adopts the same setup [36].

All models, including baselines and B-cos variants, are initialized with ImageNet-pretrained weights and fine-tuned on the target datasets. We focus on architectures with practical relevance and reasonable training cost, specifically ResNet-50 [24, 25] and ViT-B with a convolutional stem [58]. Hyperparameters are optimized using DEHB [4], separately for each architecture variant. However, for consistency, the number of training epochs is fixed across all models within the same dataset to enable direct comparisons.

To evaluate interpretability, we adapt energy-based pointing game metrics inspired by ScoreCAM [56], with minor modifications such as the removal of negative saliency values. Details of the modified metric are provided in Appendix B.

4.2. Quantitative Results

While this work includes experiments on multiple architectures, including ViT-B with a convolutional stem [58] and ConvNeXt [38], the focus here is on ResNet50-based models [24] due to their strong classification performance and practical training times. Classification metrics for both baseline and B-cos ResNet50 models across different data regimes are reported in Tab. 1. We evaluate four configurations: no augmentation, augmentation only, oversampling only, and a combination of augmentation and oversampling. Each setup is run across two random seeds, and we report the mean and standard deviation for accuracy, precision, recall, F1-score, and AUC.

A clear trend is visible in Tab. 1. Without any data augmentation or balancing, both baseline and B-cos models achieve their second-best accuracy (around 83 percent), but

Table 1. Performance metrics for **ResNet50** models on the Pneumonia Dataset with Baseline and B-cos variants. Includes different (Aug) and oversampling (Over) settings where ‘Yes’ refers to the presence of the respective method. **Bold** values indicate the best performance for each metric and underlined values indicate the second-best within a variant.

Variant	Aug	Over	Acc (%)	Pre (%)	Rec (%)	F1 (%)	AUC (%)
Baseline	No	No	<u>82.91</u> \pm 0.35	62.73 \pm 1.28	60.70 \pm 1.34	61.51 \pm 0.03	86.51 \pm 0.57
	No	Yes	79.74 \pm 0.20	53.99 \pm 0.70	74.34 \pm 1.15	62.36 \pm 0.09	86.42 \pm 0.04
	Yes	No	84.23 \pm 0.01	65.74 \pm 0.19	62.98 \pm 0.49	64.28 \pm 0.15	88.28 \pm 0.02
	Yes	Yes	81.04 \pm 0.27	55.73 \pm 0.56	77.88 \pm 0.96	64.93 \pm 0.04	87.97 \pm 0.27
B-cos	No	No	<u>82.66</u> \pm 0.07	61.47 \pm 0.13	62.55 \pm 0.81	61.88 \pm 0.43	86.50 \pm 0.04
	No	Yes	79.65 \pm 0.11	53.51 \pm 0.22	75.14 \pm 0.34	62.47 \pm 0.03	86.35 \pm 0.02
	Yes	No	83.92 \pm 0.03	65.53 \pm 0.31	61.32 \pm 0.84	63.23 \pm 0.36	87.76 \pm 0.00
	Yes	Yes	79.96 \pm 0.32	54.03 \pm 0.63	76.29 \pm 0.87	63.19 \pm 0.12	87.14 \pm 0.00

exhibit low recall and F1-score. This is problematic in clinical settings, where high recall is critical to avoid missed diagnoses [13, 40].

Introducing oversampling to balance the number of pneumonia and non-pneumonia samples results in a large increase in recall for both model types, improving by over 13 percent. However, this comes at the cost of lower precision and accuracy, highlighting the classic trade-off between detecting as many positive cases as possible and minimizing false positives [9].

Using light augmentation alone improves both accuracy and F1-score while maintaining a more balanced relationship between recall and precision. Notably, in the B-cos setting, this setup yields the highest F1-score of 63.23, demonstrating the benefit of realistic, targeted augmentation in helping models generalize better to unseen data [15].

Combining light augmentation with oversampling yields the highest recall across all setups and also leads to strong F1-scores, though again with a slight drop in precision. These performance trends are consistent across baseline and B-cos networks. The differences in performance between the two models remain within 1 to 2 percentage points, which is in line with previous findings in literature [8]. In some cases, B-cos models even outperform their baseline counterparts while offering interpretable explanations.

Compared to related work, our models outperform all prior approaches on the RSNA Pneumonia dataset with the exception of [36]. However, reproducing their results suggests that label encoding may have been reversed, casting doubt on the reliability of their reported metrics.

4.2.1 Interpretability Evaluation

Beyond classification, this work focuses on improving interpretability through the use of B-cos networks. Explanation quality is evaluated using the energy-based pointing game (EPG) metric [56], calculated with ground-truth bounding box annotations. Results are summarized in Tab. 2, comparing LayerCAM [29] on baseline networks to various B-cos

variants, with and without anti-aliasing.

Across both datasets and all training setups, the anti-aliased variant B-Cos_{FLC} consistently achieves the highest EPG scores. These improvements are particularly prominent in the VinBigData dataset, where multiple co-occurring abnormalities require explanations that are both faithful and precise.

Qualitative comparisons in Fig. 1 and Fig. 4 further confirm these findings. Explanations from baseline networks using LayerCAM tend to be diffuse or misaligned, whereas the B-cos models produce sharper, more localized contribution maps. The anti-aliased B-Cos_{FLC} variant eliminates visual artifacts and improves alignment with annotated pathology regions.

These results demonstrate that B-cos networks, particularly when combined with principled anti-aliasing using FLCPooling or BlurPool, provide clear and reliable visual explanations without sacrificing predictive performance. This makes them a compelling choice for deployment in high-stakes clinical applications.

Table 2. Energy-based pointing game results for ResNet50 B-cos networks. Compares directly the results between the inherent explanations (B-cos contribution maps) and LayerCAM explanations (post-hoc explanation) from the last convolutional layer.

Variant	Aug	Over	Method	EPG (%)	EPG TP (%)	EPG FN (%)
Baseline	No	No	LayerCAM	23.78 \pm 0.25	29.84 \pm 0.38	14.53 \pm 0.49
B-cos	No	No	LayerCAM	12.60 \pm 0.35	15.50 \pm 0.45	8.02 \pm 0.11
B-cos	No	No	Inherent Explanation	11.16 \pm 0.39	12.70 \pm 0.96	8.21 \pm 0.37
Baseline	Yes	Yes	LayerCAM	26.16 \pm 0.25	30.52 \pm 0.08	10.79 \pm 0.03
B-cos	Yes	Yes	LayerCAM	13.70 \pm 1.30	16.10 \pm 1.49	5.76 \pm 1.49
B-cos	Yes	Yes	Inherent Explanation	15.35 \pm 3.09	18.69 \pm 3.51	4.37 \pm 1.77

To better understand the limitations of standard B-cos explanations, we analyze both quantitative and qualitative results. Tab. 2 reveals a consistent presence of grid-like artifacts in B-cos models without anti-aliasing, which negatively impacts interpretability. Visual examples confirm that these artifacts disrupt alignment with clinical findings.

To address this, we evaluate anti-aliasing methods, BlurPool and FLCPooling, within the B-cos framework. As shown in Tab. 3, both approaches improve explanation quality significantly. FLCPooling in particular yields up to a 5-point improvement in EPG over baseline ResNet50 + LayerCAM, while BlurPool achieves comparable results with a smaller drop due to a slightly higher number of false negatives. However, BlurPool explanations still exhibit stronger true positive and true negative localization than the baseline LayerCAM, suggesting more faithful saliency when predictions are correct.

We also report results using recall-oriented EPG in Tab. 5. Here, the B-Cos_{FLC} model reaches a peak recall EPG of 91.56 percent, indicating high fidelity of positive contributions. A high standard deviation in this metric is linked to one fold missing several rare cases, which reduces

Table 3. Energy-based pointing game results for ResNet50 B-cos networks on threshold = 0. Compares directly the results between the inherent explanations (B-cos contribution maps) and LayerCAM explanations (post-hoc explanation) from the last convolutional layer. **Bold** values indicate the best performance, and underlined values indicate the best and second-best performing value within a metric for the corresponding pooling variant.

Variant	Aug	Over	Explanation	EPG (%)	EPG TP (%)	EPG FN (%)
B-cos	No	No	Inherent	11.16 ± 0.39	12.70 ± 0.96	8.21 ± 0.37
	No	No	LayerCAM	12.60 ± 0.35	15.50 ± 0.45	8.02 ± 0.11
	Yes	Yes	Inherent	15.35 ± 3.09	18.69 ± 3.51	4.37 ± 1.77
	Yes	Yes	LayerCAM	13.70 ± 1.30	16.10 ± 1.49	5.76 ± 1.49
B-cosFLC (ours)	No	No	Inherent	28.25 ± 1.57	39.28 ± 1.56	8.22 ± 2.10
	No	No	LayerCAM	15.62 ± 0.19	19.66 ± 0.05	8.06 ± 0.88
	Yes	Yes	Inherent	21.14 ± 0.78	25.22 ± 1.19	7.64 ± 0.74
	Yes	Yes	LayerCAM	14.62 ± 0.29	16.89 ± 0.18	7.43 ± 0.52
B-cosBP (ours)	No	No	Inherent	21.47 ± 0.27	28.36 ± 0.55	7.21 ± 0.26
	No	No	LayerCAM	16.96 ± 0.68	21.48 ± 1.37	7.76 ± 0.42
	Yes	Yes	Inherent	25.75 ± 1.17	31.14 ± 2.04	11.35 ± 0.15
	Yes	Yes	LayerCAM	22.63 ± 1.34	26.92 ± 1.96	10.95 ± 0.63

explanation quality for that split.

Table 4. Summary of the best performing Energy-based pointing game score results on the multi-label dataset

Variant	Aug	Over	EPG (%)	EPG TP (%)	EPG FN (%)
Baseline	No	No	23.78 ± 0.25	29.84 ± 0.38	14.53 ± 0.49
B-cosFLC (ours)	No	No	28.25 ± 1.57	39.28 ± 1.56	8.22 ± 2.10
Baseline	Yes	Yes	26.16 ± 0.25	30.52 ± 0.08	10.79 ± 0.03
B-cosBP (ours)	Yes	Yes	25.75 ± 1.17	31.14 ± 2.04	11.35 ± 0.15

Finally, Fig. 3 shows that explanation performance improves with increasing saliency thresholds, peaking around 0.7. This suggests that high-confidence activations from both B-cos and LayerCAM methods are well-aligned with ground-truth pathology regions, further supporting the clinical relevance of our approach.

Table 5. Recall Energy-based pointing game results on threshold t=0 across several pooling layers for ResNet50

Variant	Aug	Over	EPG (%)	EPG TP (%)	EPG FN (%)
B-cos	No	No	62.70 ± 2.25	57.88 ± 5.61	68.88 ± 0.83
B-cosFLC (ours)	No	No	78.10 ± 11.28	85.01 ± 9.66	66.16 ± 13.96
B-cosBP (ours)	No	No	83.57 ± 2.19	89.03 ± 1.41	71.46 ± 4.95
B-cos	Yes	Yes	62.37 ± 10.07	67.84 ± 8.00	43.31 ± 17.74
B-cosFLC (ours)	Yes	Yes	64.86 ± 1.50	66.03 ± 1.80	61.29 ± 1.19
B-cosBP (ours)	Yes	Yes	91.56 ± 7.97	91.38 ± 8.39	92.30 ± 6.58

The recall-based EPG analysis reveals that most activations occur at lower saliency thresholds, with scores dropping rapidly as the threshold increases. This indicates that B-cos networks, while correctly focusing on relevant regions, often include surrounding areas in their saliency maps. Whether this broader focus should be considered a limitation remains debatable, especially in clinical contexts where interpretability may benefit from contextual information.

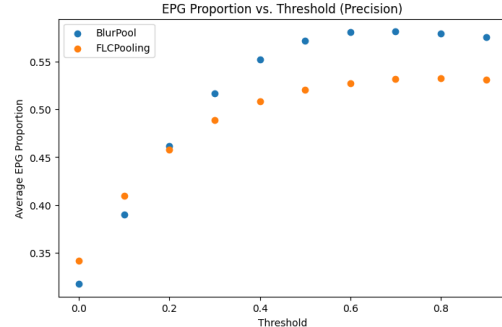


Figure 3. Energy-based pointing game result for precision with threshold. Displays best no augmentation (FLCPooling) and light augmentation (BlurPool) model

Turning to the multi-label setting, results on the VinBigData dataset are shown in Tab. 6. Our best-performing models outperform the established CheXNet [45], which achieved an F1-score of 0.435 on a comparable 14-class task. These results validate the applicability of our B-cos-based models beyond binary classification.

Table 6. Performance metrics for ResNet50 models with strided convolution using no augmentation

Variant	Acc (%)	Pre (%)	Rec (%)	F1 (%)	AUC (%)
Baseline	95.19 ± 0.03	58.44 ± 0.76	38.33 ± 0.37	43.87 ± 0.30	93.55 ± 0.04
B-cos	94.42 ± 0.33	56.44 ± 1.62	40.46 ± 2.85	43.66 ± 1.00	92.79 ± 0.20

Interestingly, while most trends from the pneumonia dataset generalize, we observe that standard strided convolutions sometimes yield better localization in the multi-label setting. This appears to be related to the tighter crop framing of the lungs in this dataset, which allows models to focus more directly on the pathology. Nonetheless, these models still suffer from the same grid artifacts, which can be misleading in clinical interpretation. The impact of these artifacts is quantified in Tab. 7, further reinforcing the value of anti-aliased B-cos variants in real-world applications.

Table 7. Energy-based pointing game results for ResNet50 B-cos networks. Compares directly the results between the inherent explanations (B-cos contribution maps) and LayerCAM explanations (post-hoc explanation) from the last convolutional layer of the baseline networks. **Bold** values indicate the best performance for each metric and underlined values indicate the second-best within a variant.

Variant	Aug	Over	Method	EPG (%)	EPG TP (%)	EPG FN (%)
Baseline	No	No	LayerCAM	22.00 ± 0.01	24.53 ± 0.66	19.62 ± 0.03
B-cos	No	No	Inherent Explanation	<u>28.02 ± 0.23</u>	<u>32.89 ± 0.44</u>	<u>25.35 ± 0.19</u>
B-cosFLC (ours)	No	No	Inherent Explanation	28.98 ± 0.00	35.99 ± 0.00	25.84 ± 0.00
Baseline	Yes	Yes	LayerCAM	22.44 ± 0.27	25.70 ± 0.60	20.75 ± 0.29
B-cos	Yes	Yes	Inherent Explanation	30.62 ± 0.06	35.33 ± 0.01	28.51 ± 0.20
B-cosBP (ours)	Yes	Yes	Inherent Explanation	<u>29.65 ± 0.44</u>	<u>34.19 ± 0.44</u>	<u>27.05 ± 0.47</u>

Finally, at threshold 0, all ResNet50 variants achieve re-

call EPG scores exceeding 99.4%, highlighting that nearly all salient activations overlap with ground-truth regions when no confidence filtering is applied.

The next section focuses on qualitative results and demonstrates how anti-aliasing improves the visual clarity and clinical usefulness of B-cos explanations.

4.3. Qualitative Results

The trends observed in the interpretability metrics are clearly reflected in qualitative examples. Figure 4 shows that B-cos models using standard strided convolutions exhibit prominent grid artifacts on the pneumonia dataset. These artifacts stem from aliasing introduced by improper downsampling [59], which can mislead interpretation in safety-critical applications.

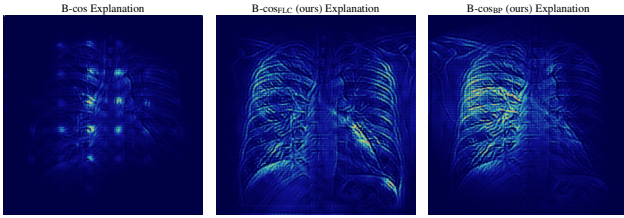


Figure 4. Comparison of B-cos explanations when using different pooling layers. **Left:** B-cos explanation, **Middle:** B-cos_{FLC} explanation, **Right:** B-cos_{BP} explanation.

Applying anti-aliasing techniques significantly improves explanation quality. The center and right images in Fig. 4, using BlurPool and FLCPooling, exhibit cleaner saliency patterns, improved localization, and sharper focus on clinically relevant regions, such as the lungs.

Similar artifacts are present in the multi-label setting, as shown in Fig. 5, where per-class B-cos explanations often contain grid noise. This suggests that aliasing is a consistent issue across datasets and configurations. Figure 6 demonstrates how BlurPool mitigates this problem by suppressing high-frequency distortions, yielding clearer and more clinically usable explanations.

In addition to evaluating raw B-cos explanations, it is instructive to compare them with post-hoc methods such as GradCAM. As shown in Fig. 7, B-cos maps capture finer structural detail and more precisely delineate the decision-relevant regions compared to GradCAM heatmaps, which often appear diffuse and ambiguous. The red bounding boxes in the unhealthy example also confirms strong alignment with disease indicators from our B-cos_{BP} model. The spatial precision of B-cos outputs can aid radiologists in verifying predictions and identifying subtle indicators of disease, making them more suited for medical decision support [8].

Nevertheless, B-cos explanations often highlight broader regions rather than sharply localized areas. While this could

be seen as a limitation, it may also reflect the network’s holistic reasoning over spatial context. The implications of this trade-off warrant further investigation.

5. Discussion

This work explores the theoretical and empirical potential of B-cos networks for chest X-ray classification. We demonstrate their suitability for medical imaging through faithful, high-quality explanations grounded in the model’s architecture [8], and show that with appropriate data augmentation, B-cos models can achieve competitive classification performance.

However, applying B-cos networks to the RSNA Pneumonia Detection Challenge [51] and VinBigData [41] datasets revealed critical limitations. First, the explanation maps were impaired by aliasing artifacts introduced by strided convolutions. Replacing them with anti-aliasing layers, such as BlurPool [59] and FLCPooling [22], resolved these artifacts and significantly improved interpretability. Second, the original B-cos implementation lacked support for multi-label classification, which is essential for datasets like VinBigData. We addressed this by extending B-cos to compute contribution maps for all output neurons.

With these modifications, B-cos networks deliver faithful, high-resolution explanations aligned with disease-relevant regions, while maintaining performance competitive with state-of-the-art models. Our metrics, including precision-based energy pointing game (EPG), confirm that over 50% of high-confidence activations fall within bounding boxes, which only cover 11.65% of the image area. These results highlight the network’s ability to focus on clinically meaningful regions. Furthermore, our models outperform LayerCAM and even CheXNet [45] on related tasks, demonstrating the value of inherent interpretability in medical AI.

Nevertheless, some limitations remain. Our focus was not on optimizing for high recall alone, as this often leads to a rise in false positives and reduced clinician trust [10]. Instead, we aimed for balanced performance across all metrics. In addition, although B-cos was evaluated on multiple architectures, models such as ConvNeXt were not extensively tested, and interpretability on ViT-B with a convolutional stem [58] was not analyzed in depth. The impact of anti-aliasing on these models remains an open question.

Looking ahead, integrating spatial priors or bounding box information into B-cos networks could enhance localization further. Another promising direction is applying B-cos models to larger datasets lacking explicit annotations to explore the trade-off between scalability and interpretability.

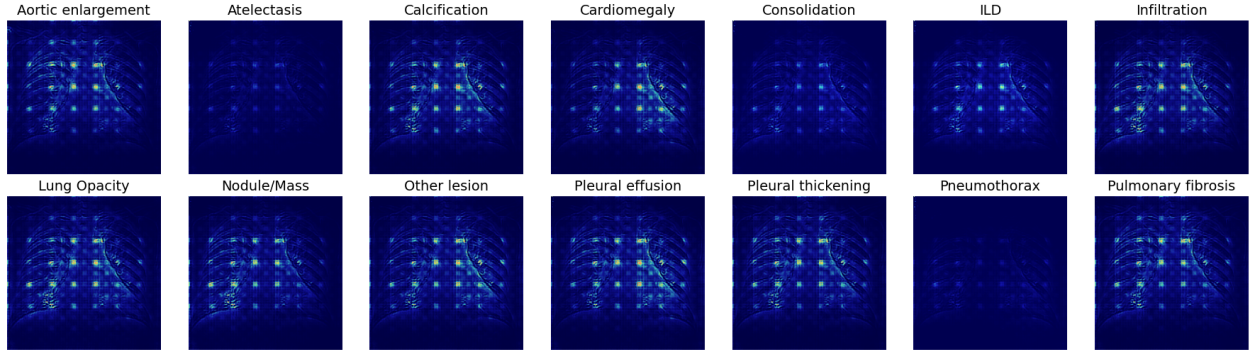


Figure 5. B-cos Multi-label explanations of a healthy patient for all fourteen abnormalities using standard B-cos models.

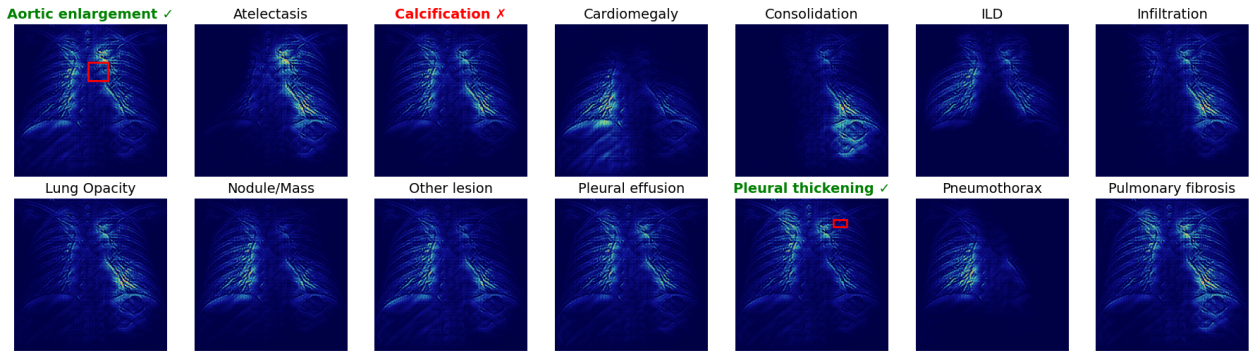


Figure 6. Multi-label explanations of an unhealthy patient who has the aortic enlargement and pleural thickening condition. B-cos_{BP} is used for these explanations, which removes the grid artifacts seen in standard B-cos networks.

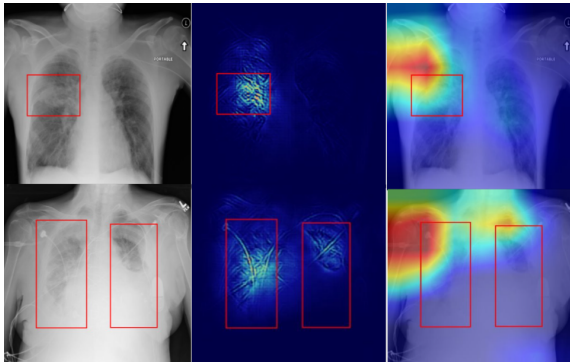


Figure 7. Comparison between GradCAM and B-cos_{BP} network explanations. From the left to the right we can see the original image, B-cos_{BP} explanation and the GradCAM heatmap over the original image for interpretability purposes. Images taken from the RSNA Pneumonia Detection Dataset [51]

6. Conclusion

This work provides a comprehensive analysis of B-cos networks for chest X-ray classification, targeting two key limitations that have restricted their application in medical imaging: aliasing artifacts in explanation maps and the lack

of support for multi-label classification. We address the former by integrating anti-aliasing techniques, FLCPooling, and BlurPool, which improve the clarity and reliability of the explanations. We address the latter by extending B-cos to produce class-wise contribution maps in multi-label settings, making the method suitable for realistic diagnostic tasks. Our experiments on the RSNA Pneumonia Detection Challenge and VinBigData Chest X-ray Abnormalities Detection datasets confirm that B-cos networks provide competitive classification performance while offering inherently interpretable, high-fidelity explanations. These explanations align closely with disease-relevant regions, as demonstrated both qualitatively and through strong energy-based pointing game scores, outperforming LayerCAM and established models such as CheXNet. By enhancing the interpretability and practical applicability of B-cos networks, this work takes an important step toward transparent and trustworthy AI-assisted diagnosis in clinical settings [61], and sets the stage for future research on scalable, interpretable deep learning for medical imaging.

Acknowledgement. S.A. and M.K. acknowledge support by the DFG Research Unit 5336 - Learning2Sense (L2S). The authors acknowledge support by the state of Baden-Württemberg through bwHPC.

References

- [1] Ravi Aggarwal, Viknesh Sounderajah, Guy Martin, Daniel S. W. Ting, Alan Karthikesalingam, Dominic King, Hutan Ashrafian, and Ara Darzi. Diagnostic accuracy of deep learning in medical imaging: a systematic review and meta-analysis. *NPJ Digital Medicine*, 4:65, Apr. 2021. [2](#)
- [2] Shashank Agnihotri, Julia Grabinski, Janis Keuper, and Margret Keuper. Beware of aliases—signal preservation is crucial for robust image restoration. *arXiv preprint arXiv:2406.07435*, 2024. [4](#)
- [3] Shashank Agnihotri, Julia Grabinski, and Margret Keuper. Improving feature stability during upsampling—spectral artifacts and the importance of spatial context. In *European Conference on Computer Vision*, pages 357–376. Springer, 2024. [4](#)
- [4] Noor Awad, Neeratyoy Mallik, and Frank Hutter. DEHB: Evolutionary Hyperband for Scalable, Robust and Efficient Hyperparameter Optimization. In *Proceedings of the Thirtieth International Joint Conference on Artificial Intelligence*, pages 2147–2153, Montreal, Canada, Aug. 2021. International Joint Conferences on Artificial Intelligence Organization. [4](#)
- [5] G Balachandran. *Interpretation of Chest X-ray: An Illustrated Companion*. Jaypee Brothers Medical Publishers, New Delhi, 1 edition, 2014. [4](#)
- [6] Alejandro Barredo Arrieta, Natalia Díaz-Rodríguez, Javier Del Ser, Adrien Bennetot, Siham Tabik, Alberto Barbado, Salvador Garcia, et al. Explainable Artificial Intelligence (XAI): Concepts, taxonomies, opportunities and challenges toward responsible AI. *Information Fusion*, 58:82–115, June 2020. [3](#)
- [7] Aurelia Bustos, Antonio Pertusa, Jose-Maria Salinas, and Maria de la Iglesia-Vayá. PadChest: A large chest x-ray image dataset with multi-label annotated reports. *Medical Image Analysis*, 66:101797, Dec. 2020. *arXiv:1901.07441 [eess]*. [3](#)
- [8] Moritz Böhle, Mario Fritz, and Bernt Schiele. B-cos Networks: Alignment is All We Need for Interpretability, May 2022. *arXiv:2205.10268 [cs]*. [2, 3, 4, 5, 7](#)
- [9] Nitesh V. Chawla, Aleksandar Lazarevic, Lawrence O. Hall, and Kevin W. Bowyer. SMOTEBoost: Improving Prediction of the Minority Class in Boosting. In Gerhard Goos, Juris Hartmanis, Jan Van Leeuwen, Nada Lavrač, Dragan Gamberger, Ljupčo Todorovski, and Hendrik Blockeel, editors, *Knowledge Discovery in Databases: PKDD 2003*, volume 2838, pages 107–119. Springer Berlin Heidelberg, Berlin, Heidelberg, 2003. Series Title: Lecture Notes in Computer Science. [5](#)
- [10] Haomin Chen, Catalina Gomez, Chien-Ming Huang, and Matthias Unberath. Explainable medical imaging AI needs human-centered design: guidelines and evidence from a systematic review. *npj Digital Medicine*, 5(1):1–15, Oct. 2022. Publisher: Nature Publishing Group. [3, 7](#)
- [11] Şeref Kerem Çorbacıoğlu and Gökhan Aksel. Receiver operating characteristic curve analysis in diagnostic accuracy studies: A guide to interpreting the area under the curve value. *Turkish Journal of Emergency Medicine*, 23(4):195–198, Oct. 2023. [13](#)
- [12] Manuel Cossio. Augmenting Medical Imaging: A Comprehensive Catalogue of 65 Techniques for Enhanced Data Analysis, Mar. 2023. *arXiv:2303.01178 [eess]*. [15](#)
- [13] David Crosby, Sangeeta Bhatia, Kevin M. Brindle, Lisa M. Coussens, Caroline Dive, Mark Emberton, Sadik Esener, et al. Early detection of cancer. *Science (New York, N.Y.)*, 375(6586):eaay9040, Mar. 2022. [5](#)
- [14] Alexey Dosovitskiy, Lucas Beyer, Alexander Kolesnikov, Dirk Weissenborn, Xiaohua Zhai, Thomas Unterthiner, Mostafa Dehghani, et al. An Image is Worth 16x16 Words: Transformers for Image Recognition at Scale, June 2021. *arXiv:2010.11929 [cs]*. [3](#)
- [15] Tatiana Gabruseva, Dmytro Poplavskiy, and Alexandr Kalinin. Deep Learning for Automatic Pneumonia Detection. In *2020 IEEE/CVF Conference on Computer Vision and Pattern Recognition Workshops (CVPRW)*, pages 1436–1443, Seattle, WA, USA, June 2020. IEEE. [3, 5, 14, 15](#)
- [16] Elisa Gentilotti, Pasquale De Nardo, Eleonora Cremonini, Anna Górska, Fulvia Mazzaferrri, Lorenzo Maria Canziani, Mona Mustafa Hellou, et al. Diagnostic accuracy of point-of-care tests in acute community-acquired lower respiratory tract infections. A systematic review and meta-analysis. *Clinical Microbiology and Infection*, 28(1):13–22, Jan. 2022. Publisher: Elsevier. [13](#)
- [17] Shantanu Ghosh, Ke Yu, Forough Arabshahi, and Kayhan Batmanghelich. Bridging the gap: From post hoc explanations to inherently interpretable models for medical imaging. In *Proceedings of the 3rd Workshop on Interpretable Machine Learning in Healthcare (IMLH) at ICML 2023*, 2023. [2, 3](#)
- [18] Leilani H. Gilpin, David Bau, Ben Z. Yuan, Ayesha Bajwa, Michael Specter, and Lalana Kagal. Explaining Explanations: An Overview of Interpretability of Machine Learning, Feb. 2019. *arXiv:1806.00069 [cs]*. [3](#)
- [19] Andrew Glassner. *Deep Learning: A Visual Approach*. No Starch Press, San Francisco, 2021. [13](#)
- [20] Rafael C. Gonzalez, Richard E. Woods, and Barry R. Masters. Digital Image Processing, Third Edition. *Journal of Biomedical Optics*, 14(2):029901, 2009. [15](#)
- [21] Ian Goodfellow, Yoshua Bengio, and Aaron Courville. *Deep Learning*. MIT Press, 2016. <http://www.deeplearningbook.org>. [13](#)
- [22] Julia Grabinski, Steffen Jung, Janis Keuper, and Margret Keuper. FrequencyLowCut Pooling - Plug and Play Against Catastrophic Overfitting. In Shai Avidan, Gabriel Brostow, Moustapha Cissé, Giovanni Maria Farinella, and Tal Hassner, editors, *Computer Vision – ECCV 2022*, pages 36–57, Cham, 2022. Springer Nature Switzerland. [2, 3, 4, 7](#)
- [23] Julia Grabinski, Janis Keuper, and Margret Keuper. Fix your downsampling ASAP! Be natively more robust via Aliasing and Spectral Artifact free Pooling, July 2023. *arXiv:2307.09804 [cs]*. [4](#)
- [24] Kaiming He, Xiangyu Zhang, Shaoqing Ren, and Jian Sun. Deep Residual Learning for Image Recognition, Dec. 2015. *arXiv:1512.03385 [cs]*. [2, 3, 4](#)

- [25] Md. Belal Hossain, S. M. Hasan Sazzad Iqbal, Md. Monirul Islam, Md. Nasim Akhtar, and Iqbal H. Sarker. Transfer learning with fine-tuned deep CNN ResNet50 model for classifying COVID-19 from chest X-ray images. *Informatics in Medicine Unlocked*, 30:100916, Jan. 2022. [2](#), [4](#)
- [26] Andrew G. Howard, Menglong Zhu, Bo Chen, Dmitry Kalenichenko, Weijun Wang, Tobias Weyand, Marco Andreetto, and Hartwig Adam. MobileNets: Efficient Convolutional Neural Networks for Mobile Vision Applications, Apr. 2017. arXiv:1704.04861 [cs]. [3](#)
- [27] Gao Huang, Zhuang Liu, Laurens van der Maaten, and Kilian Q. Weinberger. Densely Connected Convolutional Networks, Jan. 2018. arXiv:1608.06993 [cs]. [2](#)
- [28] Jeremy Irvin, Pranav Rajpurkar, Michael Ko, Yifan Yu, Silviana Ciurea-Ilcus, Chris Chute, Henrik Marklund, et al. CheXpert: A Large Chest Radiograph Dataset with Uncertainty Labels and Expert Comparison, Jan. 2019. [2](#), [3](#)
- [29] Peng-Tao Jiang, Chang-Bin Zhang, Qibin Hou, Ming-Ming Cheng, and Yunchao Wei. LayerCAM: Exploring Hierarchical Class Activation Maps for Localization. *IEEE Transactions on Image Processing*, 30:5875–5888, 2021. [1](#), [2](#), [5](#)
- [30] Alistair E. W. Johnson, Tom J. Pollard, Seth J. Berkowitz, Nathaniel R. Greenbaum, Matthew P. Lungren, Chih-ying Deng, Roger G. Mark, and Steven Horng. MIMIC-CXR, a de-identified publicly available database of chest radiographs with free-text reports. *Scientific Data*, 6(1):317, Dec. 2019. Publisher: Nature Publishing Group. [3](#)
- [31] Judith Juan, Eduard Monsó, Carme Lozano, Marta Cufí, Paula Subías-Beltrán, Laura Ruiz-Dern, Xavier Rafael-Palou, et al. Computer-assisted diagnosis for an early identification of lung cancer in chest X rays. *Scientific Reports*, 13(1):7720, May 2023. Publisher: Nature Publishing Group. [2](#)
- [32] Amirhossein Kardoost and Margret Keuper. Solving minimum cost lifted multicut problems by node agglomeration. In *Asian Conference on Computer Vision*, pages 74–89. Springer, 2018. [2](#)
- [33] Margret Keuper, Thorsten Schmidt, Marta Rodriguez-Franco, Wolfgang Schamel, Thomas Brox, Hans Burkhardt, and Olaf Ronneberger. Hierarchical markov random fields for mast cell segmentation in electron microscopic recordings. In *2011 IEEE International Symposium on Biomedical Imaging: From Nano to Macro*, pages 973–978. IEEE, 2011. [2](#)
- [34] Margret Keuper, Thorsten Schmidt, Maja Temerinac-Ott, Jan Padeken, Patrick Heun, Olaf Ronneberger, and Thomas Brox. Blind deconvolution of widefield fluorescence microscopic data by regularization of the optical transfer function (otf). In *Proceedings of the IEEE Conference on Computer Vision and Pattern Recognition*, pages 2179–2186, 2013. [2](#)
- [35] Ron Kohavi. A study of cross-validation and bootstrap for accuracy estimation and model selection. In *Proceedings of the 14th international joint conference on Artificial intelligence - Volume 2*, IJCAI’95, pages 1137–1143, San Francisco, CA, USA, Aug. 1995. Morgan Kaufmann Publishers Inc. [4](#)
- [36] Rohit Kundu, Ritacheta Das, Zong Woo Geem, Gi-Tae Han, and Ram Sarkar. Pneumonia detection in chest X-ray images using an ensemble of deep learning models. *PLOS ONE*, 16(9):e0256630, Sept. 2021. Publisher: Public Library of Science. [2](#), [3](#), [4](#), [5](#), [13](#)
- [37] Geert Litjens, Thijs Kooi, Babak Ehteshami Bejnordi, Arnaud Arindra Adiyoso Setio, Francesco Ciompi, Mohsen Ghafoorian, Jeroen A. W. M. van der Laak, et al. A survey on deep learning in medical image analysis. *Medical Image Analysis*, 42:60–88, Dec. 2017. [2](#)
- [38] Zhuang Liu, Hanzi Mao, Chao-Yuan Wu, Christoph Feichtenhofer, Trevor Darrell, and Saining Xie. A ConvNet for the 2020s, Mar. 2022. arXiv:2201.03545 [cs]. [4](#)
- [39] Dominik Müller, Iñaki Soto-Rey, and Frank Kramer. Towards a Guideline for Evaluation Metrics in Medical Image Segmentation, Feb. 2022. arXiv:2202.05273 [eess]. [2](#)
- [40] Elina Naydenova, Athanasios Tsanas, Stephen Howie, Clement Casals-Pascual, and Maarten De Vos. The power of data mining in diagnosis of childhood pneumonia. *Journal of The Royal Society Interface*, 13(120):20160266, July 2016. Publisher: Royal Society. [2](#), [5](#)
- [41] Ha Q. Nguyen, Khanh Lam, Linh T. Le, Hieu H. Pham, Dat Q. Tran, Dung B. Nguyen, Dung D. Le, et al. Vindr-cxr: An open dataset of chest x-rays with radiologist’s annotations, 2020. [3](#), [4](#), [7](#)
- [42] Luke Oakden-Rayner. Exploring large scale public medical image datasets, July 2019. arXiv:1907.12720 [eess]. [2](#)
- [43] Gabriel Iluebe Okolo, Stamos Katsigianis, and Naeem Ramzan. IEViT: An enhanced vision transformer architecture for chest X-ray image classification. *Computer Methods and Programs in Biomedicine*, 226:107141, Nov. 2022. [3](#)
- [44] Adam Paszke, Sam Gross, Francisco Massa, Adam Lerer, James Bradbury, Gregory Chanan, Trevor Killeen, et al. PyTorch: An Imperative Style, High-Performance Deep Learning Library, Dec. 2019. arXiv:1912.01703 [cs]. [14](#), [15](#)
- [45] Pranav Rajpurkar, Jeremy Irvin, Kaylie Zhu, Brandon Yang, Hershel Mehta, Tony Duan, Daisy Ding, et al. CheXNet: Radiologist-Level Pneumonia Detection on Chest X-Rays with Deep Learning, Dec. 2017. arXiv:1711.05225 [cs]. [2](#), [6](#), [7](#), [13](#), [15](#)
- [46] Vinayakumar Ravi, Vasundhara Acharya, and Mamoun Alzabab. A multichannel EfficientNet deep learning-based stacking ensemble approach for lung disease detection using chest X-ray images. *Cluster Computing*, 26(2):1181–1203, 2023. [3](#)
- [47] Mana Saleh Al Reshan, Kanwarpal Singh Gill, Vatsala Anand, Sheifali Gupta, Hani Alshahrani, Adel Sulaiman, and Asadullah Shaikh. Detection of Pneumonia from Chest X-ray Images Utilizing MobileNet Model. *Healthcare*, 11(11):1561, Jan. 2023. Number: 11 Publisher: Multidisciplinary Digital Publishing Institute. [3](#)
- [48] Cynthia Rudin. Stop explaining black box machine learning models for high stakes decisions and use interpretable models instead. *Nature machine intelligence*, 1(5):206–215, 2019. [2](#), [3](#)
- [49] Shier Nee Saw and Kwan Hoong Ng. Current challenges of implementing artificial intelligence in medical imaging. *Physica Medica: European Journal of Medical Physics*, 100:12–17, Aug. 2022. Publisher: Elsevier. [1](#)

- [50] Ramprasaath R. Selvaraju, Michael Cogswell, Abhishek Das, Ramakrishna Vedantam, Devi Parikh, and Dhruv Batra. Grad-CAM: Visual Explanations from Deep Networks via Gradient-based Localization. *International Journal of Computer Vision*, 128(2):336–359, Feb. 2020. arXiv:1610.02391 [cs]. 1, 2
- [51] George Shih, Carol C. Wu, Safwan S. Halabi, Marc D. Kohli, Luciano M. Prevedello, Tessa S. Cook, Arjun Sharma, et al. Augmenting the National Institutes of Health Chest Radiograph Dataset with Expert Annotations of Possible Pneumonia. *Radiology: Artificial Intelligence*, 1(1):e180041, Jan. 2019. Publisher: Radiological Society of North America. 3, 4, 7, 8
- [52] Amitojdeep Singh, Sourya Sengupta, and Vasudevan Lakshminarayanan. Explainable Deep Learning Models in Medical Image Analysis. *Journal of Imaging*, 6(6):52, June 2020. 3
- [53] Sukhendra Singh, Manoj Kumar, Abhay Kumar, Birendra Kumar Verma, Kumar Abhishek, and Shitharth Selvarajan. Efficient pneumonia detection using Vision Transformers on chest X-rays. *Scientific Reports*, 14(1):2487, Jan. 2024. Publisher: Nature Publishing Group. 3
- [54] Hendrik Sommerhoff, Shashank Agnihotri, Mohamed Saleh, Michael Moeller, Margret Keuper, Bhaskar Choubey, and Andreas Kolb. Task driven sensor layouts-joint optimization of pixel layout and network parameters. In *2024 IEEE International Conference on Computational Photography (ICCP)*, pages 1–10. IEEE, 2024. 13
- [55] Hugues Turbé, Mina Bjelogrlic, Christian Lovis, and Gi-anmarco Mengaldo. Evaluation of post-hoc interpretability methods in time-series classification. *Nature Machine Intelligence*, 5(3):250–260, Mar. 2023. Publisher: Nature Publishing Group. 3
- [56] Haofan Wang, Zifan Wang, Mengnan Du, Fan Yang, Zijian Zhang, Sirui Ding, Piotr Mardziel, and Xia Hu. Score-CAM: Score-Weighted Visual Explanations for Convolutional Neural Networks. In *2020 IEEE/CVF Conference on Computer Vision and Pattern Recognition Workshops (CVPRW)*, pages 111–119, Seattle, WA, USA, June 2020. IEEE. 4, 5, 13
- [57] Xiaosong Wang, Yifan Peng, Le Lu, Zhiyong Lu, Mohammad Bagheri, and Ronald M. Summers. ChestX-ray8: Hospital-scale Chest X-ray Database and Benchmarks on Weakly-Supervised Classification and Localization of Common Thorax Diseases. In *2017 IEEE Conference on Computer Vision and Pattern Recognition (CVPR)*, pages 3462–3471, July 2017. arXiv:1705.02315 [cs]. 2, 3
- [58] Tete Xiao, Mannat Singh, Eric Mintun, Trevor Darrell, Piotr Dollár, and Ross Girshick. Early Convolutions Help Transformers See Better, Oct. 2021. arXiv:2106.14881 [cs]. 4, 7
- [59] Richard Zhang. Making Convolutional Networks Shift-Invariant Again, June 2019. arXiv:1904.11486 [cs]. 2, 3, 4, 7
- [60] Fuzhen Zhuang, Zhiyuan Qi, Keyu Duan, Dongbo Xi, Yongchun Zhu, Hengshu Zhu, Hui Xiong, and Qing He. A Comprehensive Survey on Transfer Learning, June 2020. arXiv:1911.02685 [cs]. 3
- [61] Erdi Çalli, Ecem Sogancioglu, Bram van Ginneken, Kicky G. van Leeuwen, and Keelin Murphy. Deep learning for chest X-ray analysis: A survey. *Medical Image Analysis*, 72:102125, Aug. 2021. 1, 2, 8

Faithful, Interpretable Chest X-ray Diagnosis with Anti-Aliased B-cos Networks

Paper #961 Supplementary Material

Table of Contents

• Appendix A: Performance Metrics	13
This section briefly describes the performance metrics used in this work to evaluate the model performance of both B-cos and baseline networks.	
• Appendix B: Interpretability Metrics	13
Here, we explain the interpretability metrics for precision and recall used in this work.	
• Appendix C: Additional implementation details	14
In this section, we describe the model architecture, our preprocessing process, and the training process, including the necessary hyperparameters to reproduce our results.	
• Appendix D: Additional quantitative results of multi-label explanations	16
Considering the small size of the images within the main body of the paper, this section provides the images in a larger size to allow more specific analysis of the explanations while also including B-cos _{FLC} explanations that are similar to B-cos _{BP} explanations.	

A. Performance Metrics

In deep learning, there are several established metrics that are used to evaluate the performance of models. This work uses, in particular, five metrics to evaluate the performance of the respective models: accuracy [54], precision, recall, F1-score, and AUC [19, 21].

Accuracy is defined as the proportion of examples for which the model produces the correct output. While this metric is generally useful, it lacks utility for minority classes as it does not describe how many of the rare classes are predicted correctly. For instance, accuracy is a poor way to characterize the performance of a medical test that aims to detect a rare disease that occurs once in a million patients. Therefore, other metrics such as recall, precision, and F1-score are being used to evaluate unbalanced classes [21].

Precision is commonly used and defines the samples that are properly labeled positive relative to all samples that are labeled as positive. This leads to the definition of precision:

$$Precision = \frac{TP}{TP + FP}$$

where TP refers to the true positive examples and FP to the false positive examples.

Recall is also known as sensitivity and describes the percentage of the samples that are predicted to be positive relative to all samples that really are positive. This is directly described in the following equation:

$$Recall = \frac{TP}{TP + FN}$$

where TP stands for true positive and FN for false negative. As a result, it means that a recall of 1.0 describes that every positive event (e.g. disease is present) gets correctly predicted by the model while the number would be lower if a person with the disease is predicted to be healthy.

F1-score is often defined as the harmonic mean of precision and recall. Thus, the following equation determines this metric:

$$F_1 = \frac{2 \cdot Precision \cdot Recall}{Precision + Recall}$$

Therefore, it combines precision and recall into one informative metric. This leads to many authors citing the F1 score as a short way of showing that both precision and recall are high [19].

AUC is considered a summary metric of the ROC curve that reflects the test's ability to distinguish between healthy patients and patients with a disease in the medical use case. Therefore, a value of 0.5 indicates that the test has no better chance at distinguishing between the healthy and ill individuals than chance while values closer to 1.0 indicate excellent discriminatory abilities of the model. Overall, AUC

values above 0.80 are considered useful while values below 0.80 contain limited clinical utility in medical imaging [11].

All in all, these metrics are commonly used in machine learning and have relevance in medical imaging to describe model performances as seen in several sources such as [36, 45]. Despite the use of all those metrics, it is most commonly seen that recall (sensitivity) and AUC are referenced to in medical imaging tasks [16].

B. Interpretability Metrics

To evaluate the interpretability of the trained networks, it was necessary to find fitting metrics. A common method for evaluating such exact cases with bounding boxes is the energy-based pointing game presented by the Score-CAM [56] paper. It was initially used in their paper for evaluating the quality of generated saliency maps. Despite that, the method is directly applicable to our use case as the saliency map can be directly replaced with our B-cos network contribution map. Consequently, the goal is to determine how much of the energy falls into the bounding box of the target class [56]. This can be done by binarizing the input image where the bounding boxes of the target category are assigned to 1 and everything else to 0. Afterwards, there will be a point-wise multiplication of the binarization with the saliency map and sum over the whole contribution map to gain the energy in the target bounding box.

$$\frac{\sum_{(i,j) \in bbox} L^c(i,j)}{\sum_{(i,j) \in bbox} L^c(i,j) + \sum_{(i,j) \notin bbox} L^c(i,j)} \quad (1)$$

While this metric gives a vague idea of the interpretability of models by dividing the sum of the contribution map values within the bounding box divided through the sum of all contributions within the image, our experiments showed that the results can be misleading especially when analyzing poor explanations. Moreover, B-cos networks also display negative contribution values for pixels if they do not contribute positively to the class predictions. Therefore, the following extensions are introduced:

1. setting all negative values to zero which leads to the focus of the activations which contribute to the class prediction. In the formulas this is displayed by only considering L_p which are the positive contributions. This allows for comparability of the B-cos network energy-based pointing game score to baseline networks.
2. an adjustment of the metric which divides the sum of the positive values through the sum of the positive and absolute values of the negative contributions. Consequently, this metric should display whether the model sees the values inside bounding box area as primarily contributing to the class prediction.

3. using a threshold t to the existing metrics above which makes it so only values above $t \cdot \max(L_p^c)$ are considered.

The adjustments of the first two extensions lead to the following formulas where L_p references to the positive values within the contribution map and L_n to the negative values:

$$\text{precision} = \frac{\sum_{(i,j) \in \text{bbox}} L_p^c(i,j)}{\sum_{(i,j) \in \text{bbox}} L_p^c(i,j) + \sum_{(i,j) \notin \text{bbox}} L_p^c(i,j)} \quad (2)$$

$$\text{recall} = \frac{\sum_{(i,j) \in \text{bbox}} L_p^c(i,j)}{\sum_{(i,j) \in \text{bbox}} L_p^c(i,j) + \sum_{(i,j) \in \text{bbox}} |L_n^c(i,j)|} \quad (3)$$

Our adjustment to the Energy-Based Pointing Game (EPG) score in Eq. (2) transforms the calculation effectively into a precision metric by turning negative values into 0 for the B-cos networks. This directly parallels the definition of precision in a binary classification problem. In the case of only considering positive attribution values, the numerator presents true positives in the form of positive attributions located within the ground truth bounding box of the disease while the denominator represents the total positive predictions. Therefore, the denominator includes the false positive or positive values outside of the bounding box. In this case it can occur that the metric shows small values but this is also directly affected by the bounding box size. For instance, it is possible that the bounding box is only 5 or 10 percent of the image. Eq. (3) is further referenced to in this work as the recall-based energy-based pointing game score. This score is supposed to measure how much percent of the contributions within the bounding box area is positive by summing the positive values within the bounding box and divide it through the positive values summarized with the absolute value of all negative values within the bounding box. Overall, this should provide an idea whether the area within the bounding box is properly seen as an essential area by the model and how much positive contribution it has. It is worth noting that this formula takes the absolute value of the negative values. This allows for the metric to range between 0 and 1 while also considering negative contributions accordingly.

C. Additional implementation details

In this section we provide additional implementation details in regards to our network architectures based on the respective datasets.

C.1. Model Training and Architectures

Models have been trained through finetuning of pre-trained ImageNet B-cos networks published on torch [44]

and the detailed description of these networks can be found on the B-cos v2 github: <https://github.com/B-cos/B-cos-v2>.

Due to the limited pretrained models available, the goal has been to use cost efficient models which lead to the decision of ResNet50 architectures being our preferred choice due to having 25M parameters compared to the 81M of Vit-B with a convolutional stem pretrained by the authors of B-cos¹. Vit-B provides slightly better performance at the cost of using over three times the amount of parameters which leads to significantly more training time, limiting the focus on other aspects in this research. Tab. 8 shows a comparison between the performance of B-cos ResNet50 and Vit-B with a convolutional stem with different sampling and augmentation settings on one seed.

Table 8. Performance difference between B-cos ConvNeXt, Vit-B convolutional stem and ResNet50 models. **Bold** values indicate the best performance for each metric in the direct comparison under the same hyperparameters.

Variant	Aug	Over	Acc (%)	Pre (%)	Rec (%)	F1 (%)	AUC (%)
ResNet50	No	No	82.66 ± 0.07	61.47 ± 0.13	62.55 ± 0.81	61.88 ± 0.43	86.50 ± 0.04
Vit-B Conv.	No	No	83.23 ± 0.01	63.58 ± 0.31	61.68 ± 0.10	62.34 ± 0.05	87.27 ± 0.09
ReNet50	light	Yes	79.96 ± 0.32	54.03 ± 0.63	76.29 ± 0.87	63.19 ± 0.12	87.14 ± 0.00
Vit-B Conv.	light	Yes	81.51 ± 0.22	57.09 ± 0.49	73.69 ± 0.60	64.23 ± 0.08	87.78 ± 0.10

C.2. Preprocessing

Preprocessing is playing a crucial part in this work as it lead to significant improvements in performance in recall and F1-score which are essential in this field. One of the primary augmentation pipelines included augmentations that are suitable on medical data. In the following paper which focuses on the RSNA Pneumonia Detection Challenge Dataset [15], the authors introduce so-called light and heavy augmentations which lead to performance increases on object detection when it comes to this dataset. These augmentations lead to high localization within object detection and inspired our augmentation strategy as they seem plausible and dataset specific. This should lead to better localization and F1-score in particular with a potential cost in accuracy due to the stronger focus on the minority class. The augmentation strategy includes initially a normalization of the data based on the datasets mean and standard deviation to prevent large biases in the data. While this seems reasonable, this is excluded in the final implementation as the B-cos networks had worse performance analyzing accuracy and F1-score with mean and standard deviation which will be discussed in the ablation studies.

All images are being modified dynamically in the training process. First, the augmentation pipeline applies spatial transformation based data augmentations to increase model

¹Github of B-cos v2 mentions the parameter count of every pretrained model in: <https://github.com/B-cos/B-cos-v2>

robustness [15]. Initially, translation is the first augmentation that is uniformly applied and moves the image both vertically and horizontally within the range of 32 pixels. This aligns with patient positioning differences within medical applications which are likely to occur. Afterwards, this augmentation pipeline applies gaussian scaling with a scaling factor $s = 1/2^\epsilon$ where $\epsilon \in N(0, 0.1^2)$ which assists in scaling images as patients have different organ sizes. Compared to uniform scaling, this scaling peaks towards the center of the normal distribution instead of having equal amount of stronger variations. When it comes to the expectations that most organs are of similar size which applies to chest X-ray data, this can increase model generalization and robustness. In addition to translation and scaling, the augmentation pipeline applies rotation between -5 and 5 pixels while also considering a small amount of shearing of 2.5 pixels. Finally, the last spatial transformation that is applied in this image is adding randomly a perspective change of 0.1. As it would be unreasonable to add it to every image, it only gets applied to every second image. Overall, when it comes to spatial adjustments it is necessary to be conservative with these adjustments as they should be realistically applicable in practical situation [12]. It would be unreasonable to apply augmentations which are unrealistic in a clinical setting because there would be no gain in clinical applications and it might confuse models. The spatial augmentations above can realistically occur in all chest X-rays and could assist our model in learning more accurate features which can be analyzing through B-cos explanations.

Aside from the spatial transformations above, the light augmentation preprocessing includes log-normal distributed gamma correction to control luminance within images after all spatial adjustments. With this gamma correction the models should learn how to cope with lighter and darker images. This is a necessity as outside factors during the chest X-ray scan can lead to different image brightness and contrast between patients. The scale for this is defined by 2^ϵ where $\epsilon \in N(0, 0.20^2)$ where 0 is the mean and 0.2 the standard deviation. Consequently, the focus is around the peak of the gaussian distribution while some images might deviate more from the center.

Another augmentation pipeline that is applied towards pneumonia datasets is referred to as heavy augmentation with no rotation [15]. In this case, all adjustments from the light augmentation pipeline are being used with some increased adjustments in some cases. For instance, scaling and gamma correction is applied on a slightly higher standard deviation. Aside from that, there is an addition of more distorting techniques including noise based data augmentation methods [12]. In this pipeline, there is a probability to include gaussian blur, additive gaussian noise [20] and salt-and-pepper noise [20]. While this exact noise and blur additions worked best in object detection, it is interesting

to analyze how well they work in image classification with B-cos networks. Overall, this tries to test the limits of how adjusting data more thoroughly.

Our primary augmentation pipelines in light augmentation therefore focused on modifications for chest X-ray images. In the following paper which focuses on the RSNA Pneumonia Detection Challenge Dataset [15], the authors introduce so-called light and heavy augmentations which lead to performance increases on object detection when it comes to this dataset. These augmentations lead to high localization within object detection and inspired our augmentation strategy as they seem plausible and dataset-specific. This should lead to better localization and F1-score in particular with a potential cost in accuracy due to the stronger focus on the minority class.

C.3. Hyperparameter Settings

Models on the pneumonia dataset have been trained with cross-entropy loss for 30 epochs using a batch size of 16 with the Adam optimizer and the torch [44] scheduler ReduceLROnPlateau as they provide the best results based on our experiments. Nonetheless, other hyperparameters vary based on the exact models such as the learning rate and weight decay of the Adam optimizer as well as the scheduler's patience.

An overview for individual network architectures can be found in Tab. 9.

Table 9. Hyperparameter configurations across different models on the single-label pneumonia dataset.

Model	Learning Rate	Weight Decay	Patience
ResNet50 Baseline	1e-4	1e-3	3
ResNet50 B-cos	1e-5	1e-3	3
Vit-B Baseline	1e-4	1e-5	3
Vit-B B-cos	1e-5	1e-6	5

On contrast, the multi-label dataset trains only for 10 epochs and uses the following hyperparameters described in Tab. 10. It achieves better performance than CheXNet [45] despite that and retraining it with 30 epochs minimum could be beneficial in the future.

Table 10. Hyperparameter configurations across different models trained for the multi-label dataset.

Model	Learning Rate	Weight Decay	Patience
ResNet50 Baseline	1e-4	1e-3	3
ResNet50 B-cos	1e-5	1e-3	3
Vit-B Baseline	1e-4	1e-3	3
Vit-B B-cos	1e-4	1e-4	3

D. Additional qualitative results of multi-label explanations

Following, we provide larger explanations of the images given in the main paper, allowing for the observation of more details while also including B-cos_{FLC} explanations:

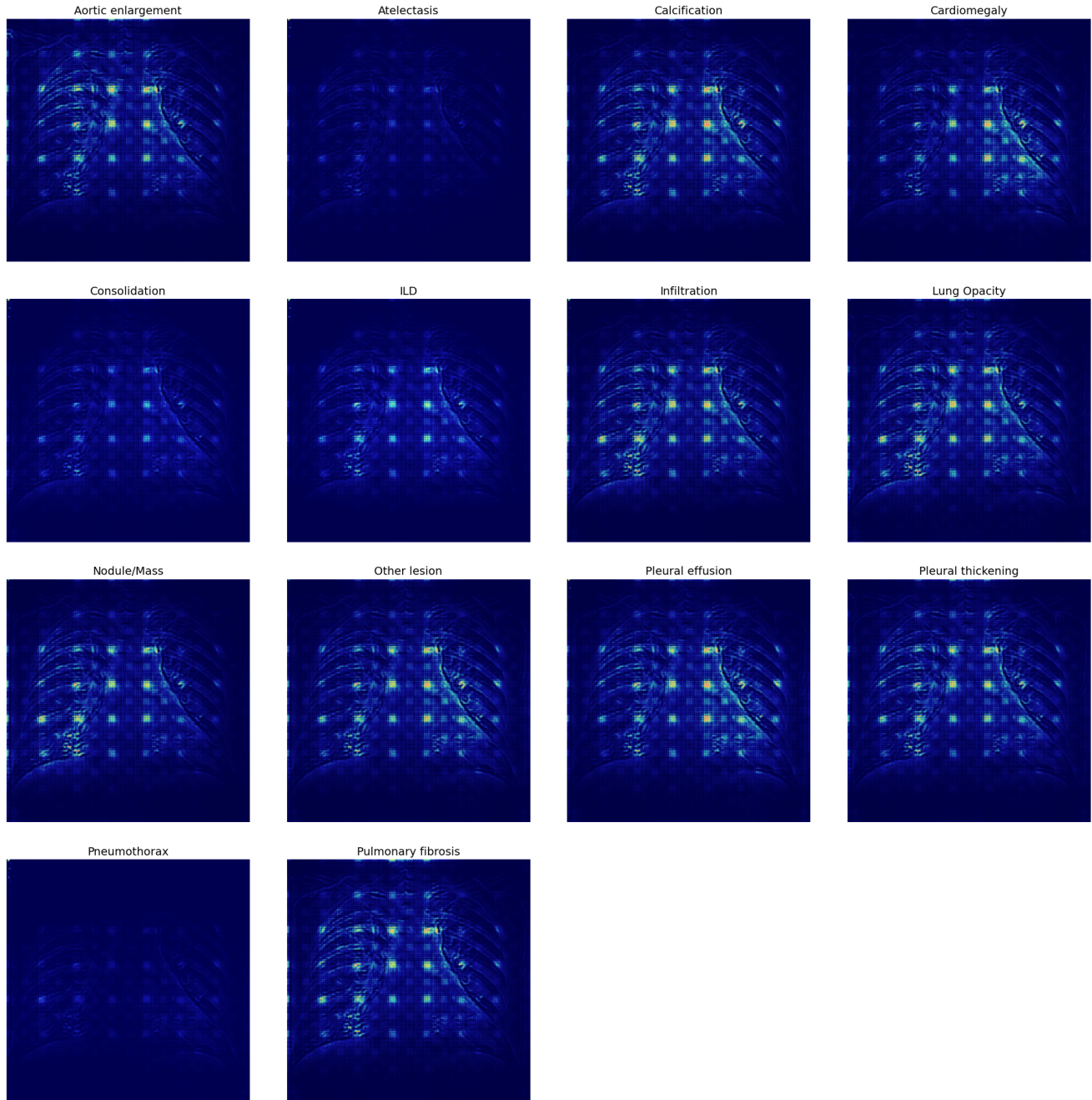


Figure 8. Multi-label explanations of a healthy patient for all fourteen abnormalities with the normal B-cos explanation.

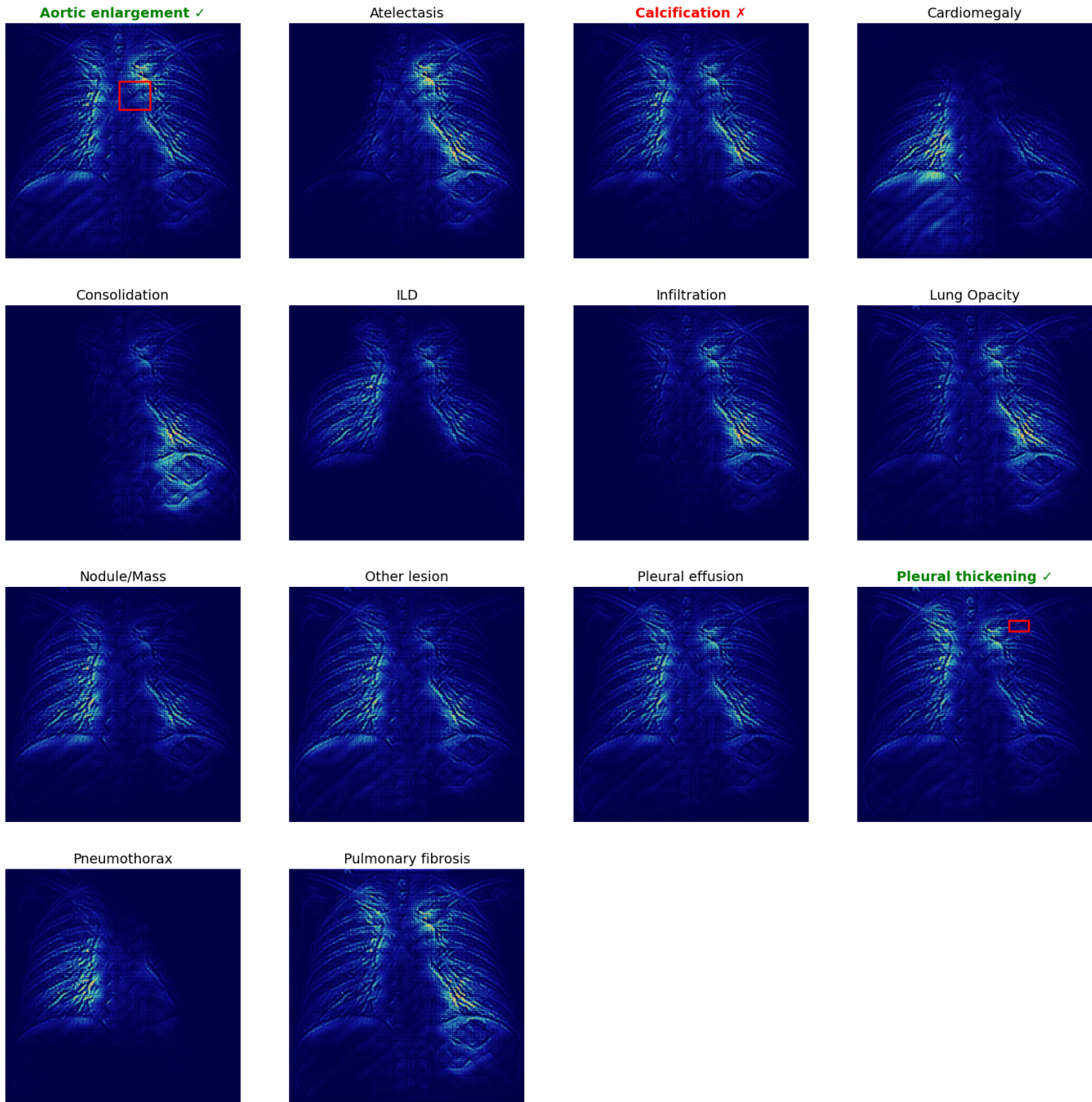


Figure 9. Multi-label explanations of an unhealthy patient that has the aortic enlargement and pleural thickening condition. B-cos_{BP} is used for these explanations which removes the grid artifacts seen in standard B-cos networks

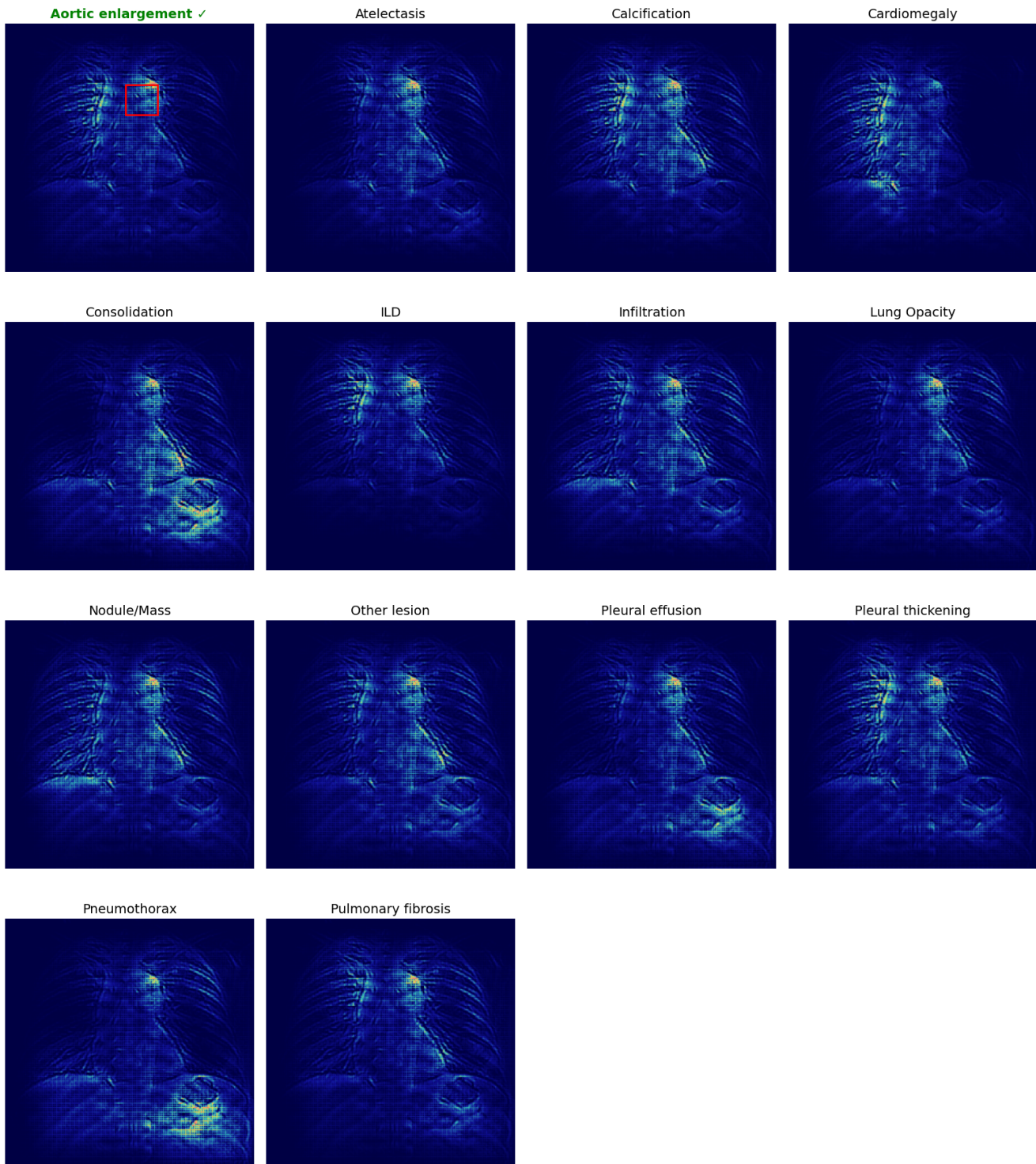


Figure 10. Multi-label explanations of an unhealthy patient that has the aortic enlargement and pleural thickening condition. B-cos_{FLC} is used for these explanations which removes the grid artifacts seen in standard B-cos networks